

Ultrananocrystalline Diamond Membranes for Detection of High-Mass Proteins

H. Kim,¹ J. Park,² Z. Aksamija,³ M. Arbulu,^{4*} and R. H. Blick^{1,5}

¹*Department of Electrical and Computer Engineering, University of Wisconsin-Madison, 1415 Engineering Drive, Madison, Wisconsin 53706, USA*

²*Department of Electrical Engineering, Kyungpook National University, Daegu 41566, Korea*

³*Department of Electrical and Computer Engineering, University of Massachusetts-Amherst, 100 Natural Resources Drive, Amherst, Massachusetts 01003, USA*

⁴*CIC-nanoGUNE, Tolosa Hiribidea 76, Donostia—San Sebastian 20018, Spain*

⁵*Center for Hybrid Nanostructures (CHyN) & Institute of Applied Physics, University of Hamburg, Jungiusstrasse 11c, 20355 Hamburg, Germany*

(Received 10 May 2016; revised manuscript received 19 August 2016; published 30 December 2016)

Mechanical resonators realized on the nanoscale by now offer applications in mass sensing of biomolecules with extraordinary sensitivity. The general idea is that perfect mechanical mass sensors should be of extremely small size to achieve zepto- or yoctogram sensitivity in weighing single molecules similar to a classical scale. However, the small effective size and long response time for weighing biomolecules with a cantilever restricts their usefulness as a high-throughput method. Commercial mass spectrometry (MS), on the other hand, such as electrospray ionization and matrix-assisted laser desorption and ionization (MALDI) time of flight (TOF) and their charge-amplifying detectors are the gold standards to which nanomechanical resonators have to live up to. These two methods rely on the ionization and acceleration of biomolecules and the following ion detection after a mass selection step, such as TOF. The principle we describe here for ion detection is based on the conversion of kinetic energy of the biomolecules into thermal excitation of chemical vapor deposition diamond nanomembranes via phonons followed by phonon-mediated detection via field emission of thermally emitted electrons. We fabricate ultrathin diamond membranes with large lateral dimensions for MALDI TOF MS of high-mass proteins. These diamond membranes are realized by straightforward etching methods based on semiconductor processing. With a minimal thickness of 100 nm and cross sections of up to $400 \times 400 \mu\text{m}^2$, the membranes offer extreme aspect ratios. Ion detection is demonstrated in MALDI TOF analysis over a broad range from insulin to albumin. The resulting data in detection show much enhanced resolution as compared to existing detectors, which can offer better sensitivity and overall performance in resolving protein masses.

DOI: [10.1103/PhysRevApplied.6.064031](https://doi.org/10.1103/PhysRevApplied.6.064031)

I. INTRODUCTION

The realization of nanomembranes with extreme lateral size generated a large demand in applications such as flexible displays, medical diagnostics, and chemical sensors [1,2]. Most of these applications focus on silicon, silicon germanium, and III-V nanomembranes [3–6]. In early work, we applied such silicon-based nanomembranes and realized their integration in matrix-assisted laser-desorption and -ionization (MALDI) time-of-flight (TOF) mass-spectrometry (MS) units for protein detection in an extremely broad mass range with unprecedented resolution [4,7,8]. The principle of detection in this case is based on thermomechanics coupled with thermally driven field emission of electrons. The aim of this work is to employ CVD diamond as a detector material due to its ultimate mechanical and specific thermal properties. Here we make use of doped diamond, which by now is commercially available at high

doping levels. In the following, we demonstrate the fabrication and application of ultrathin freestanding diamond nanomembranes for the detection of large proteins.

The schematic configuration of our MALDI TOF setup coupled with a diamond nanomembrane detector is illustrated in Fig. 1: the detector assembly is located at the exit of the time-of-flight line as in conventional MALDI TOF systems. For the measurements, we use two MALDI TOF units: a homemade system for calibration of the field emission properties and a commercial Voyager-DE 530 STR (AB SCIEX). In operation, the proteins are desorbed and ionized by a focused laser beam [9,10]. The ions are then accelerated to a final velocity depending on the mass m and charge state z by a large dc voltage (approximately 25 kV). We note that all ions possess the same energy, since this is the quantity we are detecting. The differentiation according to the m/z ratio is obtained in the TOF unit. Finally, the ions impact the backside of the freestanding diamond nanomembrane with a kinetic energy acquired in the initial acceleration stage [12]. The nanomembrane converts the kinetic

*Corresponding author.
maria@prospero-biosciences.com

energy into thermal energy and uses thermally driven field emission of electrons to detect the impact.

II. FABRICATION OF DIAMOND NANOMEMBRANES

The 100-nm-thin freestanding diamond nanomembranes are fabricated from diamond-on-insulator (DOI) materials (*Advanced Diamond Technologies, Inc., Romeoville, IL, USA*) starting from optical lithography for defining the shape of the membranes. This step is followed by an etch step, which removes the support layers [11]. An optical micrograph of the $400 \times 400 \mu\text{m}^2$ freestanding, 100-nm-thin boron-doped (*p*-type) diamond nanomembrane used in this study is displayed in the inset of Fig. 1(b). The buckling pattern [13,14] in the membrane is generated when the compressive residual stress is released [15,16] during etching out of the substrate layers within the defined square window [11].

III. ELECTROMECHANICAL CHARACTERIZATION OF NANOMEMBRANES

Before employing the nanomembrane for detection, we validate the applicability of the doped freestanding

diamond nanomembranes as field emitters. We perform a set of measurements in vacuum using the experimental configuration shown in Fig. 2(a): the electric field is ramped between the diamond nanomembrane and the extraction gate by applying voltages to the membrane (V_{DM}) and the extraction gate (V_G). Increasing the electric field reduces the energy barrier for electrons inside the diamond membrane, making it easier for electrons to tunnel out [8,17,18]. The extraction grid funnels the electrons finally to the anode. In Fig. 2(b), the *I-V* characteristic of the 100-nm-thin nanomembrane is given by red filled circles as a function of the voltage applied between the diamond membrane and extraction gate, voltage applied between the diamond membrane and extraction gate (V_{GM}).

In order to model the electron field emission analytically in this particular system, the mechanical and electrical behavior of the freestanding diamond nanomembrane need to be considered [4]. Effectively, the nanomembrane deforms due to the electromechanical pressure exerted by applying V_{GM} [11]. Hence, the electric field strength between the membrane and the extraction gate is altered. The discrepancy in the intermediate voltage range can be explained with thermionic emission [19] and Schottky emission [17,20] as shown in the inset of Fig. 2(b). The

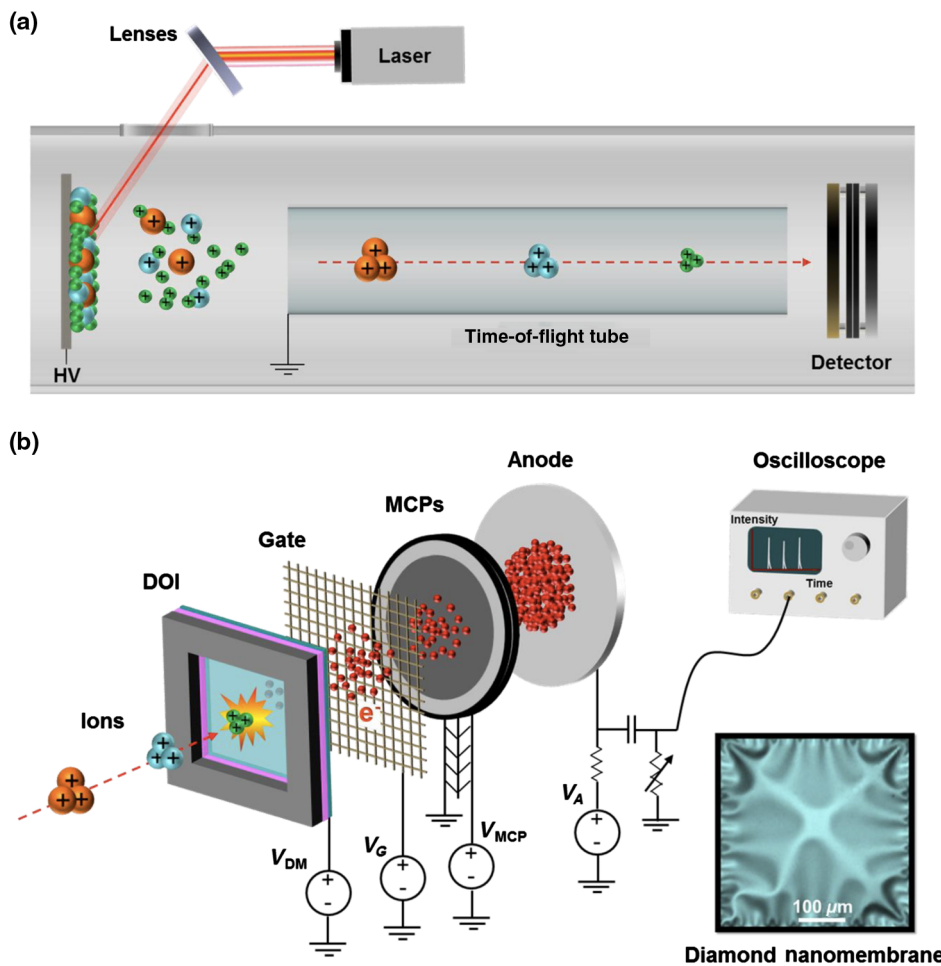


FIG. 1. The principle of operation of the diamond nanomembrane detector: (a) schematic of a MALDI TOF mass spectrometer. Proteins are desorbed and ionized by MALDI, followed by a time-of-flight separation of proteins of different mass. (b) Sketch of the detector configuration and operation principle. The detector consists of a freestanding diamond nanomembrane (receiving the kinetic energy of the impacting proteins), an extraction gate, MCP, and an anode. The electric field between the diamond nanomembrane and the extraction gate allows enhanced electron field emission by reducing the energy barrier that electrons from inside the membrane have to overcome. The MCP amplifies the number of electrons that pass through the extraction gate and arrive at the MCP. This flux of electrons is collected in the anode, and the signal is traced on the oscilloscope in the time domain. The inset shows an optical microscope image of the $400 \times 400 \mu\text{m}^2$ freestanding 100-nm-thick *p*-type diamond nanomembrane used for this study. The buckling patterns in the membrane are generated when the compressive residual stress is released during processing.

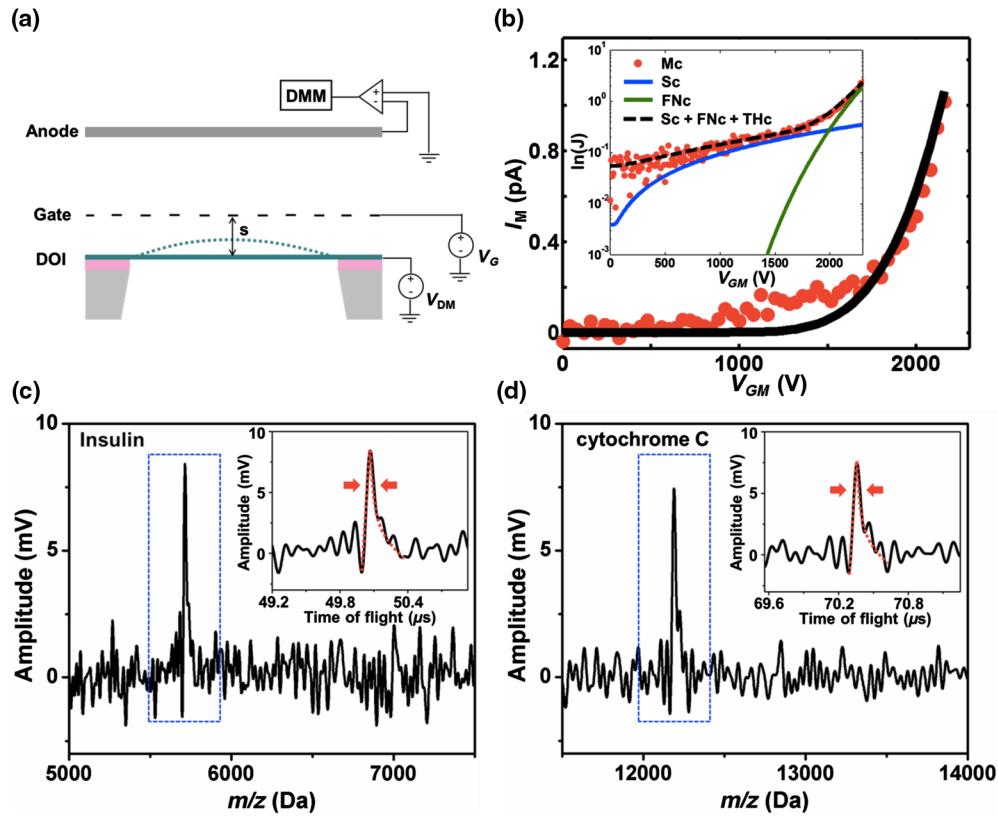


FIG. 2. Measurements with the diamond nanomembrane detector: (a) the schematic setup of the experimental configuration for field emission at room temperature. (b) Obtained data and analytical fits for field emission: the I - V curve of the measurement is given by the red filled circles, while the theoretical fit is shown as a black line. Inset: Log-scale current analysis of the three distinct mechanisms of thermionic emission (THc), Schottky emission (Sc), and Fowler-Nordheim tunneling (FNC) and comparing this to the measurement (Mc) in the intermediate voltage range. (c) and (d) show MALDI TOF mass spectra of insulin (5735 Da) and cytochrome c (12365 Da), respectively. Insets in (c) and (d): The magnified view of the recorded peaks of insulin and cytochrome c, respectively. The shape of the peaks reveal a sharp onset due to quasidiffusive transport of phonons in the out-of-plane direction (normal to the surface of the membrane) and an exponential decay by the lateral heat diffusion along in-plane direction (across the membrane) as shown in a red dashed line. The rise and decay time constants for insulin are 76.44 and 275.06 ns, respectively, while the peak of cytochrome c shows 73.36 and 265.09 ns. The peaks are very similar for both proteins since the protein concentrations, initial accelerating voltages, and, of course, the detecting nanomembranes are the same. The mass resolution ($m/\Delta m$) increases rather with increasing molecular mass. The mass resolution ($m/\Delta m$) obtained for insulin and cytochrome c is approximately 350 and approximately 480, respectively.

total emission consists of three distinct regions: the first one is at zero or at very small fields where thermionic emission acts over a barrier; the second one is the intermediate region of Schottky emission where the field is too low to cause Fowler-Nordheim (FN) tunneling [17,21–23], but it modifies the thermionic emission which works for fields up to around 10^7 V/m [17,20,24,25] (exactly the transition region in the curve); the final one is the region where FN tunneling takes over completely with fields above 10^7 V/m.

The FN equation [17] has been widely used to analyze field emission from diamond surfaces [26]. Chen *et al.* [24] developed a specific theoretical model for field emission from p -type diamond surfaces based on the theory of Stratton [27]. Following this model, the total field emission current density from a freestanding boron-doped diamond nanomembrane can be modeled by [24,25]

$$\begin{aligned}
 J &= J_c + J_v \\
 &= k_1 T^2 e^{-(\theta/kT)} e^{-k_2 \{[\chi^{(3/2)}/F]\}} + k_3 \frac{F^2}{\chi + E_g} e^{-k_2 \{[\chi + E_g]^{(3/2)}/F\}},
 \end{aligned} \tag{1}$$

where J_c and J_v are the emission current densities from the conduction band and the valence band, respectively, χ is the electron affinity, E_g is the energy gap, and θ is the energy difference between the surface conduction-band minimum and the Fermi level,

$$\begin{aligned}
 k_1 &= \frac{qm k^2}{2\pi^2 \hbar^3}, & k_2 &= \frac{4\sqrt{2m}}{3q\hbar} v(y), \\
 k_3 &= \frac{q^3}{16\pi^2 \hbar^2 t^2(y)}, & F &= \beta \frac{V_{GM}}{s(V_{GM})},
 \end{aligned} \tag{2}$$

where $v(y)$ is a tabulated function involving an elliptic integral, $t(y)$ is another tabulated function closely related to $v(y)$ [28], and $s(V_{GM})$ is obtained from the Supplemental Material [11] Eq. (S8).

Then, the total emission current from the freestanding diamond nanomembrane is proportional to the effective area of the surface and is given by $I = A_{\text{eff}} \times J$. The analytical plot of the total emission current from the $400 \times 400 \mu\text{m}^2$ freestanding 100-nm-thin diamond nanomembrane is depicted as a black line in Fig. 2(b).

Electron emission in the intermediate voltage range can be modeled as a combination of three emission mechanisms including thermionic emission, Schottky emission, and FN tunneling. Thermionic emission [19] acts primarily in the range of very small electric fields and consists of electrons being thermally excited with sufficient energy to overcome the energy barrier at the surface and, thus, being emitted into vacuum. The thermionic current is given by a well-known expression

$$J_{\text{THC}} = k_1 T^2 e^{(-\theta)/(k_B T)}, \quad (3)$$

where k_1 is the Richardson constant defined previously in Eq. (10).

Then, as the applied electric field increases, in the intermediate regime between thermionic emission and Fowler-Nordheim tunneling, a combination of the two effects occurs due to barrier lowering by the applied field. This intermediate region is where Schottky emission [20] plays a role in electron emission via modifying thermionic emission in the region where the electric field is not negligible, but it is not strong enough to cause FN tunneling:

$$J_{\text{SC}} = k_1 T^2 e^{-\{\theta - \sqrt{(F e^3 / 4\pi\epsilon_0)}\} / [k_B T]}. \quad (4)$$

In this expression, we can see how the applied electric field F defined previously in Eq. (10) reduces the height of the barrier θ at the surface. Finally, FN tunneling [17] takes over completely and dominates electron emission at fields above 10^7 V/m, which, in our setup, occurs when the applied voltage exceeds 1500 V. FN tunneling is then modeled by the modified expression given previously in Eq. (1). A log-scale current fit taking into account the three components mentioned above is shown as a black dashed line in the inset of Fig. 5(b). When combined together, Eqs. (1), (3), and (4) give a complete and accurate account of field emission from the nanomembrane. The resulting fit [a black dashed line in the inset of Fig. 2(b)] combining these three components matches the measurement data well. This exactly explains the mechanisms of field emission through the freestanding diamond membrane under applied electric fields.

IV. PROTEIN MEASUREMENTS WITH DIAMOND NANOMEMBRANES

In the next step, we use the following proteins for testing the diamond nanomembrane as a detector for MALDI TOF: insulin with mass of 5735 Da, cytochrome c at 12 365 Da, apomyoglobin at 16 952 Da, aldolase at 39 212 Da, and finally, albumin at 66 430 Da. As a matrix solution, we make use of standard sinapinic acid with mass of 224 Da (Sigma Aldrich, USA) [11]. For the measurement, we set the accelerating voltage of the ion source to a standard of 25 kV and V_{GM} , the voltage difference between the diamond nanomembrane and the extraction gate to 2.3 kV. This value is based on the previously measured field emission characteristics, as shown in Fig. 2(b).

In order to demonstrate the performance of the diamond nanomembranes as mass spectrometers, we present the detection of insulin and cytochrome c with the data sets shown in Figs. 2(c) and 2(d). The mass resolution obtained for insulin and cytochrome c is $m/\Delta m \sim 350$ and ~ 438 , respectively. The peak width Δm is defined by the standard full width at half maximum for a given mass (m). These resolutions are even better than those obtained from (i) Al/Si₃N₄/Al [4,7], where mass resolution for insulin is approximately 100 m/dm and cytochrome c is approximately 125 m/dm, (ii) a Si-nanomembrane detector [8], where mass resolution for insulin is approximately 50 m/dm and cytochrome c is approximately 75 m/dm, and (iii) standard micro channel plate (MCP) detectors (as obtained in our MALDI TOF unit for comparison) at a given mass range. This resolution indicates the improved performance of diamond nanomembranes. Figures 2(c) and 2(d) are the magnified views of the peak at the time-of-flight axis for insulin and cytochrome c, respectively. The peaks represent the sharp onset and the exponential decay as shown in a red dashed line. The rise and decay time constant at the peak are 76.44 and 275.06 ns, respectively, for insulin. The peak for cytochrome c shows 73.36 and 265.09 ns as the rise time and the decay time constant, respectively. The amplitudes of the peaks, rise times, and decay time constants in comparison are very similar for both proteins, since we dial in the same conditions such as concentration of proteins, initial accelerating high-dc voltages, and the dimension of the nanomembrane. In particular, the mass resolution ($m/\Delta m$) increases rather than decreases [29] for increased molecular masses, owing to the time resolution being similar for all masses. The response time defined with the rise and decay time constants of the peak at the time-of-flight axis results from thermal dissipation mechanisms within the membrane.

During the detection process, the nanomembrane is struck by the accelerated proteins from the MALDI TOF unit, as depicted in Fig. 1: the proteins deposit their kinetic energy onto the membrane where this energy is absorbed (thermalized), causing a heating effect. The thermodynamics of the detection process control the observed field

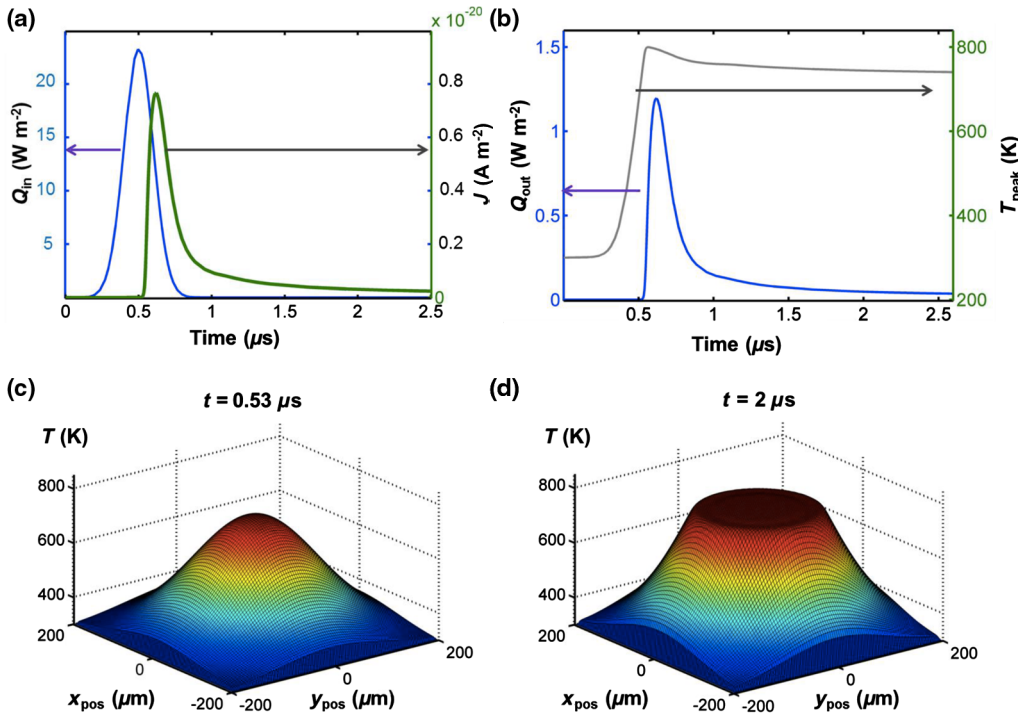


FIG. 3. Heat flux and temperature profile of the diamond nanomembrane showing a plot of the heat input (Q_{in}) caused by the impact of the proteins and the resulting field emission current J as a function of time (a). Field emission leads to an effective cooling represented by the emitted heat (Q_{out}) in (b) which limits the peak temperature of the membrane to about 800 K. The heating is initially strongest in the center, as shown by the peak in (c) obtained at $t = 0.53 \mu\text{s}$, which is the onset of the field emission current. After the field emission begins to cool the nanomembrane, the temperature profile flattens in the middle, as depicted in (d) at $t = 2 \mu\text{s}$, at the tail of the field emission peak, when the peak temperature drops below 800 K.

emission current of electrons, which is measured by the detector anode, after being accelerated by the extraction gate and amplified by the MCP. Inside the membrane, the thermal energy deposited on the backside by the proteins is described as Q_{in} in Fig. 3(a), followed by a rapid transport of that thermal energy by lattice vibrations or phonons carrying the thermal energy across the membrane [8]. Since the phonon velocity in diamond is extremely high (approximately 17 500 m/s) and the membrane thickness is smaller than the mean free path of phonons, the transit time of phonons across the 100-nm-thick membrane is very short, on the order of 10 ps and several orders of magnitude faster than either the duration of the impact of the protein cluster on the membrane or the response of the measured electron tunneling current observed in response to the MALDI TOF measurement. Following the fast transit time of quasiballistic phonons [30,31] across the membrane, the temperature at the opposite surface of the membrane rises due to the presence of additional heat-carrying phonons and causes an increase in the tunneling current of electrons due to the combined [19] thermally driven (thermionic) emission and gate-driven tunneling (field emission) effect, as shown by the peak in the field emission current density J in Fig. 3(a) and a corresponding peak in the membrane temperature T_{peak} in Fig. 3(b).

The electron current is driven by both the elevated temperature caused by heating the membrane combined with the field emission produced by the applied external field. The combination of thermionic emission and field

emission is given by Eqs. (9), (12), and (13), where the presence of the $\sim T^2 e^{-(\theta/kT)}$ term implies a strong dependence of the electron current on temperature. The membrane is, therefore, a highly sensitive thermometer, producing a large tunneling current increase in response to the heating effect by the impacting proteins. As electrons leave the membrane via tunneling, they remove energy from the membrane, causing a cooling effect [32], which is captured as Q_{out} in Fig. 3(b). The total energy removed by the field emission process is $Q_{out}(T) = EJ(T, F)/e$, where e is the electron charge, E is the electron energy, and $J(T, F)$ is the temperature- and field-dependent total electron field emission current density given by Eqs. (9), (12), and (13).

In addition to heat crossing the membrane laterally and being removed by electrons tunneling out of the membrane (Q_{out}), heat also diffuses laterally through the suspended membrane until it reaches the edges where the membrane is supported. We model the ballistic diffusive transport of phonons in the nanomembrane by decomposing the problem into the normal (ballistic) and lateral (diffusive) direction, with the lateral heat diffusion being described by the heat equation with thermal conductivity calculated from the Boltzmann transport equation using full phonon dispersion and the phonon mean free path Λ . The details of our model are given in the Supplemental Material [11] and are based on our previous work on silicon nanomembranes [8]. The resulting lateral thermal conductivity value is 12 W/(mK) at room temperature, in agreement with experimental data on nanocrystalline diamond films [33].

The low value relative to single-crystalline diamond is caused by the reduction of the phonon mean free path due to scattering at the grain boundaries [34].

The results of the numerical simulation, in particular, the electron current depicted in Fig. 3(a), match the shape, rise time of approximately 75 ns, and fall time of approximately 275 ns exhibited in the measured waveforms [shown in Figs. 2(c) and 2(d)] and show that the rise time is determined mainly by the heating process of the impacting proteins. The deposited kinetic energy heats the nanomembrane until it reaches a point where electron field emission increases and begins to cool the membrane, as evidenced by the delay between Q_{in} and Q_{out} in Figs. 3(a) and 3(b). Consequently, the rise time of approximately 75 ns depends primarily on the duration of the impact of the proteins and not on the transit time of the phonons across the membrane. The decay time is limited by the slow lateral heat diffusion, as can be seen in the change of the peak temperature T_{peak} [see Figs. 3(b)–3(d)]. The heat loss (cooling) Q_{out} via the thermionic emission of electrons is rapidly quenched due to its superexponential dependence on temperature (approximately $T^2 e^{-(\theta/kT)}$) given by Eqs. (9), (12), and (13). This strong temperature dependence of both J and Q_{out} explains the rapid initial drop in the electron tunneling current immediately following the impact of the proteins. What remains after J and Q_{out} [around 1 μ s in Figs. 3(a) and 3(b)] is a slower process of heat diffusion in the lateral direction and a radiative heat loss to the environment.

V. DISCUSSION

Based on the simulations, we conclude that the combination of the large aspect ratio, small grain structure [33,34] of the nanocrystalline diamond, and large phonon velocity combine to produce the rapid response by favoring the ballistic transport across the membrane and limiting the heat loss in the lateral direction. The main advantage of the diamond nanomembrane as compared to silicon is its enhanced thermal conductivity. As we find in analyzing the DOI material, the diamond itself consists of nanocrystalline particles in a polycrystalline matrix. These particles of about 50 nm diameter have a shape similar to rice grains and are aligned with their long axis perpendicular to the nanomembranes. Hence, heat transport in diamond nanomembranes is quite enhanced. However, the drawback is their mechanical fragility as compared to silicon and, especially, silicon nitride membranes.

In summary, we successfully demonstrate fabrication of ultrathin CVD diamond nanomembranes with extremely large cross sections, followed by analysis of residual stress. We then investigate the field emission characteristics of doped freestanding diamond nanomembranes. The analytical description of field emission provides a detailed explanation of the dominating field emission mechanisms. We finally employ the nanomembranes in a commercial

MALDI TOF mass spectrometer detecting various large proteins. The obtained data and theoretical analysis show a strongly improved sensitivity in terms of fast response time. This advanced response stems from the special thermo-mechanical characteristics of nanocrystalline CVD-grown diamond nanomembranes. This result offers the use of ultrathin doped-nanocrystalline diamond as an outstanding material for protein detection at high mass.

ACKNOWLEDGMENTS

We like to thank the Air Force Office of Scientific Research for support through the MURI'08 (Grant No. FA9550-08-1-0337). We also thank the Wisconsin Alumni Research Foundation for support via an Accelerator Program grant and the Deutsche Forschungsgemeinschaft for support via the Center for Ultrafast Imaging under Grant No. EXC-1074 (B 1.3).

-
- [1] K. Jenson, K. Kim, and A. Zettl, An atomic-resolution nanomechanical mass sensor, *Nat. Nanotechnol.* **3**, 533 (2008).
 - [2] M. S. Hanay, S. Kelber, A. K. Naik, D. Chi, S. Hentz, E. C. Bullard, E. Colinet, and L. Duraffourg, and M. L. Roukes, Single-protein nanomechanical mass spectrometry in real time, *Nat. Nanotechnol.* **7**, 602 (2012).
 - [3] J. A. Rogers, M. G. Lagally, and R. G. Nuzzo, Synthesis, assembly and application of semiconductor nanomembranes, *Nature (London)* **477**, 45 (2011).
 - [4] J. Park, H. Qin, M. Scalf, R. T. Hilger, M. S. Westphal, L. M. Smith, and R. H. Blick, A mechanical nanomembrane detector for time-of-flight mass spectrometry, *Nano Lett.* **11**, 3681 (2011).
 - [5] S. Senapati, S. Basuray, Z. Slouka, L. J. Cheng, and H. C. Chang, A nanomembrane-based nucleic acid sensing platform for portable diagnostics, *Top. Curr. Chem.* **304**, 153 (2011).
 - [6] O. Ebil, A. S. Sharkawy, M. J. Zablocki, and D. W. Prather, Chemical and biological sensors based on nanomembrane technology, *Proc. SPIE Int. Soc. Opt. Eng.* **7673**, 767308-1 (2010).
 - [7] J. Park, H. Kim, and R. H. Blick, Quasi-dynamic mode of nanomembranes for time-of-flight mass spectrometry of proteins, *Nanoscale* **4**, 2543 (2012).
 - [8] J. Park, Z. Aksamija, H. C. Shin, H. Kim, and R. H. Blick, Phonon-assisted field emission in silicon nanomembranes for time-of-flight mass spectrometry of proteins, *Nano Lett.* **13**, 2698 (2013).
 - [9] W. C. Wiley and I. H. McLaren, Time-of-flight mass spectrometer with improved resolution, *Rev. Sci. Instrum.* **26**, 1150 (1955).
 - [10] K. Tanaka, H. Waki, Y. Ido, S. Akita, Y. Yoshida, and T. Yoshida, Protein and polymer analyses up to m/z 100,000 by laser ionization time-of-flight mass spectrometry, *Rapid Commun. Mass Spectrom.* **2**, 151 (1988).
 - [11] See Supplemental Material at <http://link.aps.org/supplemental/10.1103/PhysRevApplied.6.064031> for

- theoretical aspects of nanomembrane fabrication and additional mass spectra.
- [12] G. C. Hilton, Impact energy measurement in time-of-flight mass spectrometry with cryogenic microcalorimeters, *Nature (London)* **391**, 672 (1998).
- [13] T. Kramer and O. Paul, Postbuckled micromachined square membranes under differential pressure, *J. Micro-mech. Microeng.* **12**, 475 (2002).
- [14] A. Evans, M. Prestat, R. Tölke, M. V. F. Schlupp, L. J. Gauckler, Y. Safa, T. Hocker, J. Courbat, D. Briand, N. F. De Rooij, and D. Courty, Residual stress and buckling patterns of free-standing yttria-stabilized-zirconia membranes fabricated by pulse laser deposition, *Fuel Cells* **12**, 614 (2012).
- [15] M. J. Madou, *Fundamentals of Microfabrication: The Science of Miniaturization* (CRC Press, Boca Raton, FL, 2002).
- [16] J. A. Thornton and D. Hoffman, Stress-related effects in thin films, *Thin Solid Films* **171**, 5 (1989).
- [17] R. H. Fowler and L. Nordheim, Electron emission in intense electric fields, *Proc. R. Soc. A* **119**, 173 (1928).
- [18] R. Stratton, Theory of field emission from semiconductors, *Phys. Rev.* **125**, 67 (1962).
- [19] C. A. Mead, Operation of tunnel-emission devices, *J. Appl. Phys.* **32**, 646 (1961).
- [20] F. Seitz, *F. Modern Theory of Solid* (McGraw-Hill Book Company, New York, 1940), Vol. 2, pp. 161–168.
- [21] T. Yamada, H. Yamaguchi, K. Okano, and A. Sawabe, Field emission properties of boron- and phosphorus-doped diamond, *New Diamond Front. Carbon Technol.* **15**, 337 (2005).
- [22] P. T. Joseph, N. H. Tai, C. H. Chen, H. Niu, H. F. Cheng, and I. N. Lin, On the mechanism of enhancement on electron field emission properties for ultrananocrystalline diamond films due to ion implantation, *J. Phys. D* **42**, 105403 (2009).
- [23] S. P. Bozeman, P. K. Baumann, V. L. Ward, M. J. Powers, J. J. Cuomo, R. J. Nemanich, and D. L. Dreifus, Electron emission measurements from CVD diamond surfaces, *Diam. Relat. Mater.* **5**, 802 (1996).
- [24] C. L. Chen, C. S. Chen, and J. T. Lue, Field emission characteristic studies of chemical vapor deposited diamond films, *Solid State Electron.* **44**, 1733 (2000).
- [25] S. Y. Chen and J. T. Lue, Temperature dependence of surface band bending and field emission for boron-doped diamond and diamond-like films, *New J. Phys.* **4**, 79 (2002).
- [26] T. Yamada, H. Yamaguchi, K. Okano, and A. Sawabe, Field emission properties of boron- and phosphorus-doped diamond, *New Diamond Front. Carbon Technol.* **15**, 337 (2005).
- [27] R. Stratton, Theory of field emission from semiconductors, *Phys. Rev.* **125**, 67 (1962).
- [28] H. C. Miller, Values of Fowler-Nordheim field emission functions, *J. Franklin Inst.* **282**, 382 (1966).
- [29] X. Chen, M. S. Westphall, and L. M. Smith, Mass spectrometric analysis of DNA mixtures: Instrumental effects responsible for decreased sensitivity with increasing mass, *Anal. Chem.* **75**, 5944 (2003).
- [30] M. E. Siemens, Q. Li, R. Yang, K. A. Nelson, E. H. Anderson, M. M. Murnane, and H. C. Kapteyn, Quasi-ballistic thermal transport from nanoscale interfaces observed using ultrafast coherent soft x-ray beams, *Nat. Mater.* **9**, 26 (2010).
- [31] W. E. Bron, Y. B. Levinson, and J. M. O'Connor, Phonon Propagation by Quasidiffusion, *Phys. Rev. Lett.* **49**, 209 (1982).
- [32] M. S. Chung, S. C. Hong, A. Mayer, P. H. Cutler, B. L. Weiss, and N. M. Miskovsky, New analysis of electron energy exchange and cooling in semiconductors, *Appl. Phys. Lett.* **92**, 083505 (2008).
- [33] H. Verhoeven, A. Floter, H. Reiss, R. Zachai, D. Wittorf, and W. Jäger, Influence of the microstructure on the thermal properties of thin polycrystalline diamond films, *Appl. Phys. Lett.* **71**, 1329 (1997).
- [34] M. N. Touzelbaev and K. E. Goodson, Application of micron-scale passive diamond layers for the integrated circuits and microelectromechanical systems industries, *Diam. Relat. Mater.* **7**, 1 (1998).